Functional Renal Imaging with 2-Deoxy-2-^{18}F-Fluorosorbitol PET in Rat Models of Renal Disorders

Rudolf A. Werner[1–3], Hiroshi Wakabayashi[1,4], Xinyu Chen[1,3], Mitsuru Hirano[1,3], Tetsuya Shinaji[1,3], Constantin Lapa[1], Steven P. Rowe[2], Mehrbod S. Javadi[2], and Takahiro Higuchi[1,3,5]

[1]Department of Nuclear Medicine, University Hospital Würzburg, Würzburg, Germany; [2]Division of Nuclear Medicine and Molecular Imaging, Russell H. Morgan Department of Radiology and Radiological Science, Johns Hopkins University School of Medicine, Baltimore, Maryland; [3]Comprehensive Heart Failure Center, University Hospital Würzburg, Würzburg, Germany; [4]Department of Nuclear Medicine, Kanazawa University, Kanazawa, Japan; and [5]Department of Bio-Medical Imaging, National Cerebral and Cardiovascular Research Center, Suita, Osaka, Japan

The best indicator of kidney function is considered to be the glomerular filtration rate (GFR). However, because the filtration process occurs simultaneously in millions of glomeruli, a direct measurement of GFR is not feasible (*1*). The filtered agent ^{99m}Tc-diethylenetriaminepentaacetic acid (^{99m}Tc-DTPA) is widely available as a means to determine split GFR estimation by plotting dynamic renogram time–activity curves from planar images. However, precise regional assessment of renal function is limited by this 2-dimensional approach. Furthermore, Compton scatter and soft-tissue attenuation are major obstacles for reliable quantification. The use of hybrid imaging devices such as SPECT/CT enables 3-dimensional anatomic coregistration; however, the prolonged SPECT acquisition time and the limited temporal resolution reduce the potential of dynamic imaging (*2*).

Dynamic tomographic imaging with PET has the intrinsic advantage of high temporal and spatial resolution when compared with the 2-dimensional planar approach used with single-photon imaging agents. Furthermore, as previously confirmed in an experimental study on healthy rats, the PET radiotracer 2-deoxy-2-^{18}F-fluorosorbitol (^{18}F-FDS) has emerged as a promising candidate for measuring renal function with high kidney extraction and excretion, low plasma protein binding, and high metabolic stability (*3*). Given the simple 1-step reduction of the most frequent PET radiotracer, ^{18}F-FDG, the use of ^{18}F-FDS might open the window to the clinical availability of renal PET imaging.

The purpose of the present study was to elucidate the imaging and kinetic characteristics of ^{18}F-FDS for the assessment of renal function in renally impaired rats using models of acute renal failure (ARF) and unilateral ureteral obstruction (UUO).

MATERIALS AND METHODS

Radiotracer Production

^{18}F-FDS was synthesized by following a previously described procedure (*4*). In short, $NaBH_4$ (2 mg, 0.053 mmol) was added to a solution of ^{18}F-FDG in saline, and the resulting mixture was stirred at 35°C for 15 min. After quenching of the reaction, the mixture was adjusted to a pH of 7.4 and filtered through an Alumina-N Sep-Pak cartridge (Waters). The filtrate was then reconstituted in saline and passed through a 0.22-μm Millipore filter into a sterile multidose vial. A radiochemical purity of more than 95% was confirmed for ^{18}F-FDS by radio–thin-layer chromatography (CR 35 Bio; Raytest) (80% acetonitrile with 20% water as eluent) (*3*).

For correspondence or reprints contact: Takahiro Higuchi, Department of Nuclear Medicine/Comprehensive Heart Failure Center, University Hospital Würzburg, Oberdürrbacher Strasse 6, 97080 Würzburg, Germany.
E-mail: thiguchi@me.com

DTPA kits (Fujifilm RI Pharma) were labeled using generator-produced ^{99m}Tc-pertechnetate according to the manufacturer's instructions.

Animal Preparation

Male Wistar rats weighing 200–250 g (n = 18) were used. Experimental protocols were approved by the regional governmental commission of animal protection and conducted in strict accordance with the *Guide for the Care and Use of Laboratory Animals* published by the U.S. National Institutes of Health (*5*). ARF was induced by intramuscular injection of 50% glycerol (10 mL/kg) in each hind leg after a 24-h water deprivation period (n = 5) (*6,7*). At 24 h after glycerol injection, experimental tracer studies were conducted. UUO was induced by complete ligation of the left ureter near the renal pelvis (n = 9) (*8*). At 24 h after the ligation procedure, experimental studies were performed. As controls, experimental studies were also performed on 4 healthy rats.

Small-Animal PET Imaging

The rats were studied with a high-resolution dedicated small-animal PET system (Inveon microPET; Siemens Healthcare) (*9*). They were maintained under anesthesia by 2% isoflurane during the entirety of the experiments. ^{18}F-FDS (30 MBq) was administered via the tail vein for PET imaging, and ^{99m}Tc-DTPA (2 MBq) was coinjected for reference for urine γ-counting and autoradiography. The 30-min list-mode scan was started just before radiotracer injection. The list-mode data were sorted into 3-dimensional sinograms, which were then rebinned with fully 3-dimensional binning to reconstruct dynamic images using 3-dimensional ordered-subset expectation maximization. The reconstructed dynamic images consisted of 56 acquired frames (15 frames × 8 s, 26 frames × 30 s, and 15 frames × 60 s).

The obtained PET images were analyzed using an image-processing application (AMIDE imaging software, version 1.0.1) (*10*). Three-dimensional regions of interests were manually drawn over the entire kidney, including the medulla. The mean concentration of radioactivity within the regions of interests was expressed as the percentage injected dose per cubic centimeter of tissue. Time–activity curves (renography) were generated, and the time points of maximal (T_{max}) and half-maximal ($T_{½max}$) concentration were computed.

Postmortem Analysis

For γ-counting, plasma was collected via the tail artery during the PET acquisition (10 min after tracer delivery). After the PET acquisition (35 min after tracer injection), the rats were euthanized, urine was collected by opening the abdominal cavity, and autoradiography studies were conducted. Plasma (4 ARF rats, 4 controls) and urine (3 ARF rats, 3 controls) were counted for radioactivity in an automated γ-counter (Wizard; PerkinElmer). The radioactivity concentrations, expressed as percentage injected dose per gram, were calculated (*3*). The kidneys were frozen and cut into 20-μm short-axis slices using a cryostat (Leica). Dual-radiotracer autoradiography was performed to assess both ^{18}F-FDS and ^{99m}Tc-DTPA uptake. First, the imaging plate (MultiSensitive Phosphor Screens; PerkinElmer) was exposed for 3 h to visualize the distribution of ^{18}F-FDS with a digital autoradiography system (CR 35 Bio; Raytest). After 18 h to allow for the decay of ^{18}F, a second exposure for 12 h was started to evaluate ^{99m}Tc-DTPA uptake. After autoradiography, tissue slices were stained with hematoxylin and eosin.

Statistics

All results are displayed as mean ± SD. The 2-tailed paired Student t test was used to compare differences between 2 dependent groups, and the 2-tailed independent Student t test was used to compare differences between independent groups. For correlative analyses, Pearson coefficients of correlation were calculated. A P value of less than 0.05 was considered statistically significant. Statistical analysis was done with StatMate III (ATMS Co., Ltd.) and JMP (SAS Institute Inc.).

RESULTS

Small-Animal Imaging

Whole-body dynamic PET imaging demonstrated high radiotracer excretion via the kidneys, with a low hepatobiliary clearance in control animals (Figs. 1 and 2). Blood flow through the inferior vena cava and the arterial vasculature was visualized, followed by a gradual delineation of the renal cortex and transition of the activity into the collecting system and renal pelvis (Fig. 1A). Visual analysis demonstrated that ^{18}F-FDS was excreted solely through the urinary system and subsequently transited into the bladder. No obvious signals from other organs were detected (Fig. 1B). A normal renogram pattern consistent with blood-flow, parenchymal, and excretory phases, with a T_{max} of 1.1 ± 0.6 min and a $T_{½max}$ of 12.2 ± 3.0 min, was derived in control rats (Fig. 1C, top). As expected, the bladder demonstrated a continuous radiotracer increase in control rats (Fig. 1C, bottom).

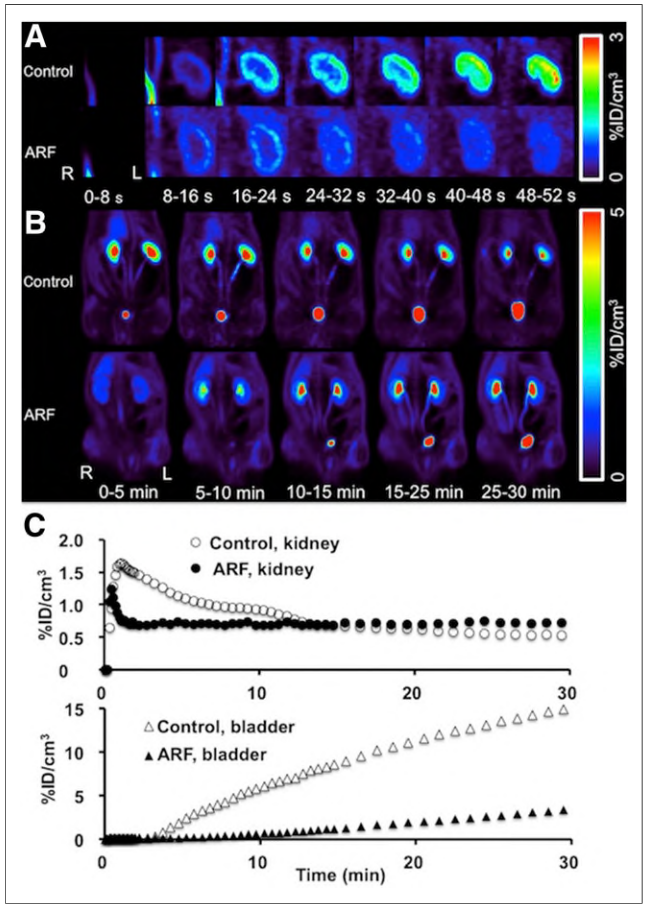

FIGURE 1. (A) Coronal dynamic ^{18}F-FDS PET images of left kidney show rapid cortical uptake in control rat but reduced cortical uptake in ARF rat. (B) Coronal dynamic whole-body ^{18}F-FDS PET images show control rats to have high tracer secretion exclusively via kidneys and time-dependent increase in bladder activity, whereas ARF rats have reduced tracer secretion via kidneys and delayed increase in bladder activity. (C) Average time–activity curves for kidneys and bladder by dynamic PET (averaged T_{max} of kidneys in ARF rats, 0.5 ± 0.1 min) show low tracer secretion via kidneys in ARF rats. %ID = percentage injected dose.

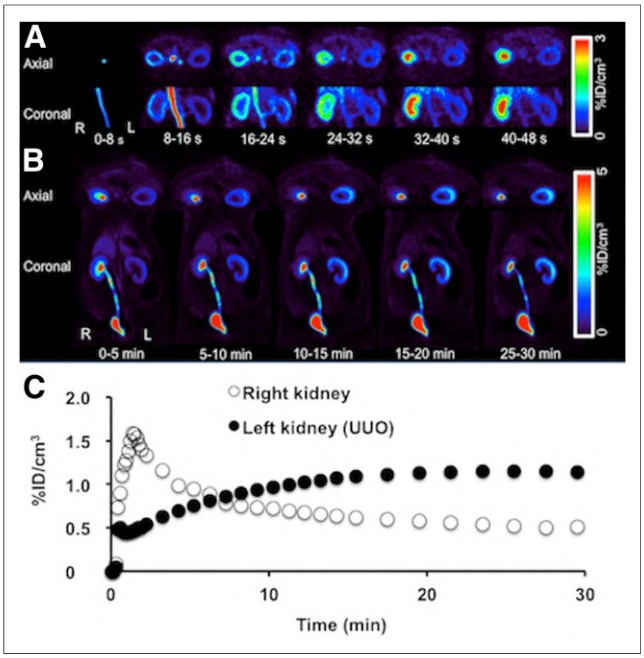

FIGURE 2. (A) Dynamic ^{18}F-FDS PET images of UUO rats show reduced cortical uptake in affected kidney but rapid cortical uptake in contralateral kidney. (B) Dynamic whole-body ^{18}F-FDS PET images show affected kidney to have time-dependent increase in uptake but no tracer excretion, whereas tracer is seen in pelvis of contralateral kidney at 0–5 min. (C) Average time–activity curves for kidneys by dynamic PET (averaged T_{max} of kidneys in UUO rats, 22.7 ± 4.5 min) show tracer deposition in cortex of affected kidney. %ID = percentage injected dose.

On PET images, uptake in the renal cortex was significantly less in ARF rats than in controls (Fig. 1A), and radiotracer excretion through the urinary system was lower. In particular, radiotracer transit to the bladder was delayed (Fig. 1B). These findings were further corroborated using averaged radiotracer time–activity curves. The derived renograms showed a nonfunctioning pattern, indicating that glomerular filtration was impaired after glycerol injection (Fig. 1C, top). T_{max} was 0.5 ± 0.1 min in ARF rats ($P < 0.05$, vs. controls), whereas $T_{½max}$ was not reached during the 30-min scan. Additionally, bladder activity was reduced and delayed in the ARF model (Fig. 1C, bottom).

In UUO rats, enlarged PET images of the renal area displayed a weak to moderate radiotracer retention in the renal cortex over time (Fig. 2A). Lower and delayed uptake was observed on the obstructed side, with no transition into the collecting system and renal pelvis (Fig. 2B, left kidney), whereas the contralateral side (Fig. 2B, right kidney) showed results similar to those obtained in control rats. The derived renograms demonstrated a typical pattern for an obstructed kidney: on averaged time–activity curves, the increase in activity on the obstructed side was slow, with no further peak during the parenchymal phase and progressive parenchymal accumulation (Fig. 2C). For the UUO kidneys, T_{max} was 22.7 ± 4.5 min ($P < 0.0001$ vs. controls), whereas $T_{½max}$ was not reached.

γ-Counting and Autoradiography Results

On γ-counting, the ^{18}F-FDS concentrations in plasma ($R = 0.77$) and urine ($R = 0.84$) correlated well with the ^{99m}Tc-DTPA concentrations ($P < 0.05$, Table 1). Autoradiography confirmed a similar renal distribution for both radiotracers in control and ARF rats (Fig. 3). With regard to the hematoxylin and eosin staining, retained radioactivity was observed in the inner medullary collecting ducts.

TABLE 1
Plasma and Urine Concentrations of Coinjected ^{18}F-FDS and ^{99m}Tc-DTPA on γ-Counting Studies

Site	^{18}F-FDS	^{99m}Tc-DTPA
Plasma	0.16	1.15
	0.15	0.43
	0.21	0.25
	0.3	0.89
	0.7	1.22
	0.4	1.35
	0.5	1.62
	0.72	2.23
Urine	6.8	20.9
	2.3	6.2
	4.4	4.6
	1.7	5.7
	1.4	3.8
	2.7	4.8

Data are percentage injected dose per gram.

In Vivo Stability and Plasma Protein Binding

Radio–thin-layer chromatography analysis of rat plasma samples and ^{18}F-FDS solution revealed completely matched single spots in all samples from each group ($n = 2$), indicating the nonexistence of radiolabeled metabolites in blood 30 min after radiotracer administration. In vivo serum protein binding of ^{18}F-FDS at 30 min after radiotracer administration was quantified as minimal (<0.1%) by separation of free ^{18}F-FDS using ultrafiltration.

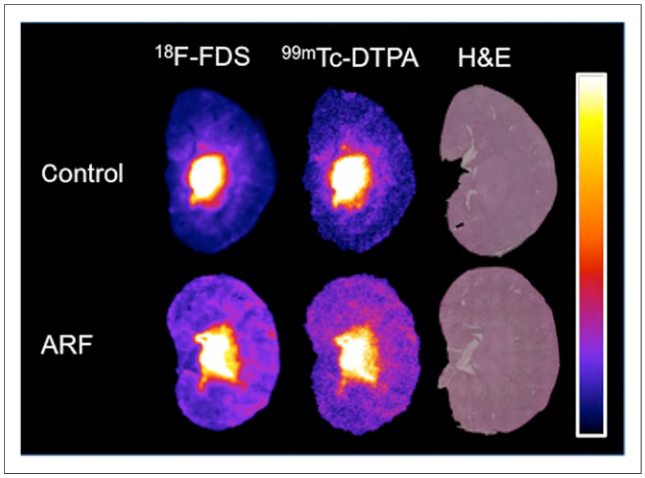

FIGURE 3. Coronal autoradiography slices of kidney show comparable distribution pattern for ^{18}F-FDS and ^{99m}Tc-DTPA in both control and ARF rats. High radioactivity was observed in inner medulla on hematoxylin- and eosin-stained (H&E) sections.

DISCUSSION

As the standard of renal function measurement, GFR assessment requires an exogenous marker that behaves similarly to inulin, that is, free filtration without any tubular secretion or absorption (*11*). Suitable exogenous markers for measuring renal function, such as ^{51}Cr-EDTA, are widely used in clinical practice, and plasma clearance estimated by multiple blood samples increases its diagnostic accuracy, although repeated sampling makes it inconvenient (*11*). GFR estimation using ^{99m}Tc-DTPA planar imaging is biased by the applied method of scintigraphic GFR determination (*12*), and camera-based techniques depend on the precise assessment of renal depth for soft-tissue attenuation corrections (*13*). On the other hand, recent efforts have been made to develop novel renal imaging agents focusing on tubular function and renal plasma flow instead of measuring GFR (*14,15*). With kinetics identical to the gold standard ^{131}I-orthoiodohippurate for measurement of effective renal plasma flow, ^{99m}Tc-$(CO)_3$(fluoroethyl)iminodiacetic acid inherits the advantage of improved background activity correction; however, none of the methodology currently in place is able to solve this issue successfully (*16,17*). In contradistinction, as previously demonstrated in healthy rats and confirmed in the present study, ^{18}F-FDS allows for almost complete elimination of background activity from surrounding organs (*3*). We observed rapid excretion via the urinary system (without visualized hepatobiliary clearance), high in vivo stability, and low serum protein binding. Furthermore, in 2 different rat models of kidney disease, functional impairment of the injured kidneys was successfully identified: in ARF rats, radiotracer extraction by and excretion through both kidneys was low, and radiotracer accumulation in the bladder was minimal. Imaging-derived renograms showed a bilateral nonfunctioning pattern. In the UUO rat model, radiotracer extraction from the blood pool was reduced, and transit from the cortex to the collecting system in the obstructed kidney was significantly impaired. Renograms demonstrated a typical obstructed pattern on the affected side.

In the present dual-tracer autoradiography study using the γ-camera imaging agent ^{99m}Tc-DTPA and the PET tracer ^{18}F-FDS, biodistribution for the two radiotracers was comparable. However, renal PET imaging offers numerous advantages, such as increased spatiotemporal resolution and accurate tomographic 3-dimensional quantitative capability (*17*). As a competitor for PET renal imaging, ^{68}Ga-EDTA was recently introduced as a substitute for ^{99m}Tc-DTPA (*18*). Compared with its ^{68}Ga-labeled counterpart, ^{18}F-FDS provides a cost-effective approach toward radiotracer production by a simple 1-step reduction of ^{18}F-FDG, and its longer half-life allows for flexibility in study design. Further, it possesses the inherent advantages of lower positron energy along with higher positron yield. Strikingly, as an analog of sorbitol, ^{18}F-FDS has kinetic properties that are theoretically identical to the gold standard inulin (sorbitol–to–inulin clearance ratio, 1.01) (*19*). However, regardless of which radiotracer is used, the major obstacle of renal PET imaging in a human setting has to been addressed—that is, current PET cameras do not allow imaging of the entire urinary system in a single field of view (*18*). Hence, it might be necessary to use costly large-field whole-body PET devices or to obtain multiple PET and CT acquisitions, which might hamper diagnostic accuracy.

In light of radiation exposure and higher costs, the clinical situation in which its use in renal radionuclide imaging would be most justified remains a matter of debate. A decade ago, renovascular hypertension and kidney transplant rejection were seen as major clinical indications for renal PET; however, improvements in drug development and the widespread availability of nonradiation methods such as ultrasound have led to a massive decline in such study requests in recent years (*20–23*). Currently, common clinical indications include monitoring during chemotherapy or assessment of split renal function for various clinical indications, such as before radiotherapy or before live kidney donation (*24–26*). Because of the superior spatial and temporal resolutions of PET, ^{18}F-FDS could potentially be applied in those clinical situations, especially for determining differential glomerular filtration.

In view of the promising results of recently published randomized clinical trials, treatment of inoperable, metastasized neuroendocrine tumors with radiolabeled somatostatin analogs is currently gaining ground (*27*). However, renal irradiation from peptide receptor radionuclide therapy is most likely to be caused by cross fire of radiolabeled somatostatin analogs from adjacent tubules, and it was hypothesized that serial ^{99m}Tc-mercaptoacetyltriglycine studies might be a superior indicator for early stages of kidney dysfunction caused by endoradiotherapy (*28*). However, measurement of tubular extraction rate was unsuitable as an early way to identify an increased probability of later renal failure (*29*). Hence, a dual-radiotracer approach using somatostatin receptor PET together with ^{18}F-FDS PET could potentially be applied to patients scheduled for peptide receptor radionuclide therapy and replace common renography studies in the long term.

Most importantly, creatinine clearance–based estimates of GFR are often used in pediatrics. However, changes in body mass limit the reliability of this method, and accuracy is hampered in children with renal and urologic disorders (*17*). Moreover, children can also have anatomic abnormalities of the kidney, such as ureteropelvic junction obstruction (*30*). Ideally, in these difficult clinical situations, ^{18}F-FDS renal PET might set the scene for effective decision making, as it provides simultaneous information about anatomic conditions and about the functional significance of an obstruction (*17*). Given the increased count rates obtained with ^{18}F-FDS, as compared with conventional imaging agents such as ^{99m}Tc-DTPA, a much lower activity of ^{18}F can be administered. Hence, mainly because of the advantages of PET over SPECT, ^{18}F-FDS could potentially minimize radiation exposure in children without sacrificing image quality. Moreover, when a PET/CT study is performed, the additional radiation exposure from the CT component should also be considered. However, use of a low-dose or ultra–low-dose CT scan along with the narrow field of view necessary for renal imaging could further lower radiation exposure to less than 0.25 mSv (*2*).

CONCLUSION

In 2 rat models of kidney disease, ^{18}F-FDS PET demonstrated favorable kinetics for functional renal imaging. Renal PET/CT has the potential to provide improved spatial and temporal functional data when the clinical situation does not allow relevant information to be easily obtained by other common noninvasive techniques. Because of its superior diagnostic performance and simple production via reduction of ^{18}F-FDG, ^{18}F-FDS might meet this urgent need in renal radionuclide imaging. Strikingly, ^{18}F-FDS could potentially minimize radiation exposure in children without sacrificing image quality. Further confirmatory studies in humans are warranted.

DISCLOSURE

This work was supported by the Competence Network of Heart Failure funded by the Integrated Research and Treatment Center (IFB) of the Federal Ministry of Education and Research (BMBF) and the German Research Council (DFG grant HI 1789/3-3). This project received funding from the European Union's Horizon 2020 research and innovation program under Marie Sklodowska-Curie grant agreement 701983. Hiroshi Wakabayashi received a JSPS Grant-in-Aid for Research (17K10353). No other potential conflict of interest relevant to this article was reported.

REFERENCES

1. Soveri I, Berg UB, Bjork J, et al. Measuring GFR: a systematic review. *Am J Kidney Dis.* 2014;64:411–424.
2. Hofman MS, Hicks RJ. Gallium-68 EDTA PET/CT for renal imaging. *Semin Nucl Med.* 2016;46:448–461.
3. Wakabayashi H, Werner RA, Hayakawa N, et al. Initial preclinical evaluation of ^{18}F-fluorodeoxysorbitol PET as a novel functional renal imaging agent. *J Nucl Med.* 2016;57:1625–1628.
4. Li ZB, Wu Z, Cao Q, et al. The synthesis of ^{18}F-FDS and its potential application in molecular imaging. *Mol Imaging Biol.* 2008;10:92–98.
5. *Guide for the Care and Use of Laboratory Animals.* 8th ed. Washington, DC: National Academy Press; 2011.
6. Singh AP, Junemann A, Muthuraman A, et al. Animal models of acute renal failure. *Pharmacol Rep.* 2012;64:31–44.
7. Westenfelder C, Arevalo GJ, Crawford PW, et al. Renal tubular function in glycerol-induced acute renal failure. *Kidney Int.* 1980;18:432–444.
8. Tantawy MN, Jiang R, Wang F, et al. Assessment of renal function in mice with unilateral ureteral obstruction using ^{99m}Tc-MAG3 dynamic scintigraphy. *BMC Nephrol.* 2012;13:168.
9. Disselhorst JA, Brom M, Laverman P, et al. Image-quality assessment for several positron emitters using the NEMA NU 4-2008 standards in the Siemens Inveon small-animal PET scanner. *J Nucl Med.* 2010;51:610–617.
10. Loening AM, Gambhir SS. AMIDE: a free software tool for multimodality medical image analysis. *Mol Imaging.* 2003;2:131–137.
11. Gaspari F, Perico N, Remuzzi G. Measurement of glomerular filtration rate. *Kidney Int Suppl.* 1997;63(suppl):S151–S154.
12. Mulligan JS, Blue PW, Hasbargen JA. Methods for measuring GFR with technetium-99m-DTPA: an analysis of several common methods. *J Nucl Med.* 1990;31:1211–1219.
13. Taylor A, Lewis C, Giacometti A, Hall EC, Barefield KP. Improved formulas for the estimation of renal depth in adults. *J Nucl Med.* 1993;34:1766–1769.
14. Lipowska M, Klenc J, Jarkas N, Marzilli LG, Taylor AT. Monoanionic ^{99m}Tc-tricarbonyl-aminopolycarboxylate complexes with uncharged pendant groups: radiosynthesis and evaluation as potential renal tubular tracers. *Nucl Med Biol.* 2017;47:48–55.
15. Klenc J, Lipowska M, Taylor AT. Synthesis and evaluation of ^{99m}Tc$(CO)_3$ (FEDA): a new dual-purpose ^{99m}Tc/^{18}F renal imaging agent [abstract]. *J Nucl Med.* 2015;56(suppl 3):654.
16. Blaufox MD. Renal background correction and measurement of split renal function: the challenge. *Eur J Nucl Med Mol Imaging.* 2016;43:548–549.
17. Blaufox MD. PET measurement of renal glomerular filtration rate: is there a role in nuclear medicine? *J Nucl Med.* 2016;57:1495–1496.
18. Hofman M, Binns D, Johnston V, et al. ^{68}Ga-EDTA PET/CT imaging and plasma clearance for glomerular filtration rate quantification: comparison to conventional ^{51}Cr-EDTA. *J Nucl Med.* 2015;56:405–409.
19. Willie W, Smith HF, Smith HW. Renal excretion of hexitols (sorbitol, mannitol, and dulcitol) and their derivatives (sorbitan, isomannide, and sorbide) and of endogenous creatinine-like chromogen in dog and man. *J Biol Chem.* 1940;135:231–250.
20. Szabo Z, Xia J, Mathews WB, Brown PR. Future direction of renal positron emission tomography. *Semin Nucl Med.* 2006;36:36–50.
21. Taylor AT. Radionuclides in nephrourology, part 2: pitfalls and diagnostic applications. *J Nucl Med.* 2014;55:786–798.
22. Textor SC. Current approaches to renovascular hypertension. *Med Clin North Am.* 2009;93:717–732.
23. Hanssen O, Erpicum P, Lovinfosse P, et al. Non-invasive approaches in the diagnosis of acute rejection in kidney transplant recipients. Part I. In vivo imaging methods. *Clin Kidney J.* 2017;10:97–105.
24. Delbeke D, Segall GM. Status of and trends in nuclear medicine in the United States. *J Nucl Med.* 2011;52(suppl 2):24S–28S.
25. Jackson P, Foroudi F, Pham D, et al. Short communication: timeline of radiation-induced kidney function loss after stereotactic ablative body radiotherapy of renal cell carcinoma as evaluated by serial ^{99m}Tc-DMSA SPECT/CT. *Radiat Oncol.* 2014;9:253.
26. Hartlev LB, Boeje CR, Bluhme H, Palshof T, Rehling M. Monitoring renal function during chemotherapy. *Eur J Nucl Med Mol Imaging.* 2012;39:1478–1482.
27. Strosberg J, El-Haddad G, Wolin E, et al. Phase 3 trial of ^{177}Lu-dotatate for midgut neuroendocrine tumors. *N Engl J Med.* 2017;376:125–135.
28. Sabet A, Ezziddin K, Pape UF, et al. Accurate assessment of long-term nephrotoxicity after peptide receptor radionuclide therapy with ^{177}Lu-octreotate. *Eur J Nucl Med Mol Imaging.* 2014;41:505–510.
29. Werner RA, Beykan S, Higuchi T, et al. The impact of ^{177}Lu-octreotide therapy on ^{99m}Tc-MAG3 clearance is not predictive for late nephropathy. *Oncotarget.* 2016;7:41233–41241.
30. Williams B, Tareen B, Resnick MI. Pathophysiology and treatment of ureteropelvic junction obstruction. *Curr Urol Rep.* 2007;8:111–117.